Reactive sputtering onto an ionic liquid, a new synthesis route for bismuth-based nanoparticles

Sara Ibrahim, Vitalios Ntomprougkidis, Mathias Goutte, Guillaume Monier, Mounir Traïkia, Jean-Michel Andanson, Pierre Bonnet, Angelique Bousquet

ARTICLE

Reactive Sputtering onto an Ionic Liquid, A New Synthesis Route of Bismuth-Based Nanoparticles

Received 00th January 20xx,
Accepted 00th January 20xx

DOI: 10.1039/x0xx00000x

Sara Ibrahim [a], Vitalios Ntomprougkidis [a], Mathias Goutte [a], Guillaume Monier [b], Mounir Traïkia [a], Jean-Michel Andanson [a], Pierre Bonnet [a], Angelique Bousquet *[a]

Metallic bismuth and Bi-oxyfluoride nanoparticles (NPs) are successfully synthesized by non-reactive and reactive sputtering of a Bi target onto 1-butyl-3-methylimidazolium bis(trifluoro-methylsulfonyl)imide ([BMIM][TFSI]) ionic liquid (IL). Non-reactive sputtering is realized in pure Ar plasma, where isotropic, well crystallized and dispersed Bi NPs of 3-7 nm are obtained. The diameter and the size distribution of these NPs do not significantly vary with the power, gas pressure, and sputtering time; but these sputtering parameters seem to influence the NPs concentration. Then, the introduction of O_2 and CF_4 gases in addition to Ar enables the reaction of radicals from plasma with Bi clusters at the liquid top surface to form Bi-oxyfluoride NPs of 3-12 nm in diameter with a photocatalytic activity. Hence, the reactive sputtering onto an IL is an efficient, original and promising method for synthesizing Bi-based compound NPs. Finally, we propose a mechanism based on reactions of species from plasma at the IL surface to explain the formation of Bi-compounds by reactive sputtering.

1. Introduction

Nanoparticles (NPs) are particles of matter with a diameter of less than 100 nm. They have attracted significant attention from the materials science community due to their unique physical properties. The applications of NPs depend profoundly on their size. The large surface-to-volume ratio and the quantum confinement effect are the significant factors, which enhance the application of NPs in diverse areas, including optics, electronics, biomedicine, catalysis, and solar energy conversion.[1] The synthesis of NPs can be accomplished by chemical and physical methods. The chemical methods include Chemical Vapour Deposition [2–4] and colloidal synthesis. [5–7] In the Chemical Vapour Deposition process, NPs are obtained from a volatile precursor as a consequence of one or more chemical reactions in the gas phase. In contrast, the colloidal synthesis method involves reactions between the reactants in the solution. The chemical methods are versatile and allow controlling the size of NPs, but they necessitate costly metal salt and result in the formation of by-products and NPs with definite purity. [1] On the other hand, the physical methods are clean and do not change the initial chemical composition. Therefore, the obtained nanoparticles are of similar purity to that of the initial material. The physical synthesis involves mainly laser-based techniques and sputtering. From one hand, the laser-based techniques require photons to ablate a target into a gas or into a liquid media, where the NPs will be formed. From the other hand, sputtering is usually achieved via a solid substrate, where the atoms nucleate and grow at the surface of the substrate, forming a thin film. So far, sputtering onto liquid substrates represented a new, efficient and simple method to prepare metallic NPs. [1] The non-volatile liquid substrates include vegetable oils [8], polymers liquids, and ionic liquids (ILs). [9–13] The first sputtering deposition onto a liquid substrate occurred in 1996 via the RF magnetron sputtering silver onto pure silicone oil. [14] A power lower than 30 W allowed the formation of Ag nanoparticles inside the oil, while a higher power enabled obtaining a continuous and thin Ag film at the surface. Yet, the nanoparticles were neither identified nor characterized because the interest at that time was to obtain a metallic film. However, this approach has opened tremendous opportunities for scientists to work with different liquid substrates for synthesizing high-quality NPs with advanced properties. In 1999, Wagener successfully prepared Fe and Ni magnetic NPs of 9 nm and Ag NPs of 5-15 nm in diameter by sputtering metallic targets onto liquid surfaces. [15] Hence, it was the first time to synthesize metallic colloidal nanoparticles in silicone oil by sputtering. However, the obtained colloids were not stable since silicone lacks a functional group to firmly anchor the particle surfaces and stabilize NPs. [16] Accordingly, the use of another stable liquid substrate for sputtering NPs without the addition of a stabilizer was indispensable. In 2006, Torimoto *et al.* introduced an IL as a substrate in vacuum sputtering. [12] Therefore, Torimoto et al. and other groups realized the synthesis of noble metal NPs involving Au, Ag, Pd, and Pt with high colloidal stability. [12,17–19] As a consequence, the optical and plasmonic properties of noble metal nanoparticles (principally Au and Ag) were thoroughly investigated. Less

[a] *Université Clermont Auvergne, Clermont Auvergne INP, CNRS, Institut de Chimie de Clermont-Ferrand, F-63000 Clermont–Ferrand, France.*
[b] *Université Clermont Auvergne, Clermont Auvergne INP, CNRS, Institut Pascal, F-63000 Clermont–Ferrand, France.*
Electronic Supplementary Information (ESI) available: [details of any supplementary information available should be included here]. See DOI: 10.1039/x0xx00000x

information is available on non-noble metal or semimetal nanoparticles.

Recently, Bi-metal NPs have shown a direct plasmonic response, ascribed to the synergetic effect of SPR phenomenon. [20–22] So, bismuth nanoparticles have been widely used in different photocatalytic applications but were never synthesized by sputtering onto IL. Moreover, in such field, Bi-based compounds, like oxide or oxyfluorides, were also investigated as valuable photocatalytic materials. [23, 24] For applications in photocatalysis, it is then crucial to control the materials' composition and to nanostructure them to increase their specific surface area. Hence, it would be particularly interesting to be able to form nanoparticles not only of metallic Bismuth, but also of Bi-based compounds, taking advantage of the high versatility of the reactive sputtering techniques in material composition control. However, up to now, only few papers reported the formation of compound materials by sputtering on IL. Carette *et al.* obtained Titanium oxide (TiO_2) NPs by post-oxidation in air of metallic Ti NPs formed via sputtering a titanium target onto pentaerythritol ethoxylate (PEEL). [25] Akiyoshi et al. synthesized molybdenum oxide NPs thanks to a controlled post-heating in air of Mo NPs formed by ionic liquid/metal sputtering. [26] Other authors introduce a constant and high O_2 flow rate during sputtering, which progressively poisoned the target by an oxide and then modifies the process with time. Authors then collected NPs into IL at different stages of this continuously changing process. [27] More recently, Meischein *et al* obtained partially oxyded copper NPs by introducing a moderate O_2 reactive gas during the sputtering of a copper target, in order to maintain it in metallic state. [28] This reactive sputtering experiments mainly aim to compare with non-reactive mode to understand NPs formation mechanisms. The originality of our work arises in trying to synthesize NPs of Bismuth oxyfluorides into IL by a controlled addition of various mixtures of reactive gases (O_2 and CF_4). In this paper, we will first synthesize NPs by sputtering a Bi target in pure Ar atmosphere. We then add O_2 and CF_4 to form oxyfluoride NPs. Their photocatalytic ability for methyl orange degradation is tested to highlight the interest of such NPs. In order to better understand the interaction between plasma and IL, we also study the IL exposure to plasma in various atmospheres without NPs production. Finally, we try to propose a mechanism to explain the NPs formation in this specific reactive sputtering process.

2. Experimental section

The plasma process reactor used is an Alliance Concept EVA 300+ equipment. It is composed of a deposition chamber containing two magnetron targets facing a rotatable substrate holder and four microwave applicators. The targets were supplied by a 13.56 MHz radiofrequency power through matching boxes, while the additional applicators received a 2.45 GHz microwave power. The injected gas flow rates were controlled by calibrated mass flow meters within the range of 0 to 30 standard cubic centimeters per minute (sccm). The pumping system consisted of a dry primary pump and a secondary turbo molecular pump that allows to reach a base pressure close to 10^{-6} mbar. A network of three gauges (Pirani, Baratron and Penning) enabled us to follow the pressure inside the reactor at all processing stages: from atmospheric pressure to the residual vacuum and during the plasma experiments.

The [BMIM][TFSI] (1-butyl-3-methylimidazolium bis(trifluoromethanesulfonyl)imide) IL with a purity of 99 % was purchased from Iolitec. The IL was first purified under vacuum at 10^{-1} mbar for at least 24 hours. This purification step allows the removal of water absorbed from the ambient air in the IL. Then, a Karl-Fischer titration was performed, where the quantities of water were obtained below 50 ppm (0.005 % by mass of water). IL is often defined as a salt with a melting point below the boiling point of water, consisting entirely of ions. ILs have a very low vapor pressure [29] which allows them to be used in the plasma chamber under a high vacuum. A (100 x 15 mm) petri dish containing 3.5 ml of IL was placed on a support in front of the target in the chamber. We used a Bi target (99.99 % purity from Neyco) of 7.6 cm in diameter. Before sputtering, we left the IL under residual vacuum (close to 10^{-6} mbar) for a long time, where it remained stable, and bubbles were not observed.

For NPs formation, a pure Bi target was sputtered in argon plasma with a power (P) of 50 W, an argon flow rate (Φ_{Ar}) of 30 sccm, which was equivalent to a working pressure of 2.3×10^{-2} mbar, and a sputtering time (t_s) of 20 min or 3 hours. After that, the sputtering parameters were varied to investigate their impact on the concentration and suspension of the obtained Bi NPs. Next, the effect of O_2 and CF_4 as reactive gases was investigated by sputtering the bismuth target in $Ar/O_2/CF_4$ mixtures. In this study to form oxyfluoride compounds, we chose to introduce fluorine via CF_4 gas rather than F_2 which is a simpler but more dangerous gas. It is important to notice that, to be reproducible, experiments in reactive sputtering should follow a precise process, already explained in previous works. [23] Prior to any synthesis, the target was sputtered in pure Ar plasma (Φ_{Ar} = 30 sccm) at 50W in order to remove any compound at the target surface. This step of at least 30 min lasted until the target self-bias voltage reached the value corresponding to a metallic target. Then, the $Ar/O_2/CF_4$ gas mixture was introduced with the plasma lighted on in the studied conditions for few minutes in order to stabilize the target surface and the entire reactor. Finally, the shutter was removed to start the NPs synthesis. For comparison with NPs, metallic and Bismuth oxyfluorides in powder were also synthesized by chemical routes, following these references [30,31] respectively.

To investigate the effect of plasma on the IL, without sputtering the bismuth target, we used a microwave plasma supply. 30 sccm of argon was introduced and a voltage of 3 V, which is equivalent to 360 W, was applied to allow Ar plasma illumination through the four applicators (90 W through each applicator), placed at 7 cm from the IL Petri dish. Then, in addition to Ar, the injection of O_2 or/and CF_4 gases enabled obtaining different plasmas containing reactive species. To

highlight the potential modifications of the IL, the plasma exposure time was fixed to 1 hour. The plasma was investigated by optical emission spectroscopy (OES), accompanied by the HORIBA Scientific system. The measurements were done in the range of 200–850 nm using an iHR 320 monochromator and an intensified CCD camera.

After plasma treatment, the IL solutions containing NPs or modified by the plasma were poured into a quartz cell (10 mm path length, quality 6Q from Hellma) and analysed by UV-visible spectroscopy using a JASCO V-650 device. IR and Nuclear Magnetic Resonance (NMR) spectroscopies were used to estimate the degradation of the IL. For the most intense bands (anion), the IR spectrum was recorded in Attenuated Total Reflectance (ATR), while for the less intense bands, the signal's intensity was increased by measuring the spectrum in transmission (CH stretching of the cation). ^{1}H, ^{13}C, ^{15}N and ^{19}F NMR spectra of the IL before and after plasma process were also recorded.

When we synthesized NPs, they were directly analysed by TEM and HR-TEM, putting a small drop of dispersion solution on grid, or they were extracted from IL for other chemical analysis techniques. Both protocols for TEM grid preparation and NPs extraction from IL are annexed in supporting information.

The morphology of the particles was monitored using a Hitachi H7650 transmission electron microscope (TEM) with an acceleration voltage of 80 kV. Then, the size distribution of the nanoparticles was determined after analysing the images with ImageJ software. Moreover, high-resolution TEM (HR-TEM) images, selected-area electron diffraction (SAED) and Energy Dispersive Spectroscopy (EDS) were carried out in "Centre de microcaractérisation Raimond Castaing" Toulouse with JEOL JEM 2100F and acceleration voltage of 200 kV.

After their extraction from IL, the crystal structure of the NPs was investigated by X-ray diffraction, PANalytical XPert'PRO diffractometer model (Cu Kα1 1.5406 Å, Cu Kα2 1.5444 Å, 40 kV, 30 mA, and an angle step of 0.0167°). Their chemical composition and environment were determined by X-ray photoelectron spectroscopy (XPS) using the Omicron brand EA 125 model with a DAR 400 X source. The following utilizes the Mg Kα anode (E = 1253.6 eV) and a hemispheric analyser working at constant energy of 20 eV for the acquisition of high-resolution spectra. A high-resolution measurement was made for Bi 4f, O 1s, F 1s, S 2p and C 1s peaks. After the acquisition, the exploitation of the experimental data was carried out by the XPSPEAK41 software. First, a Shirley baseline was used to subtract the background level on the spectra. After, even if the shift of peaks position is moderate, a charge correction is necessary to find the "true" energy position of the different XPS signals. For this purpose, the position of the binding energy of carbon sp^2 at 284.6 eV, originated from the IL, is taken as a reference for powder and NPs extracted from LI and of carbon sp^3 at 285.4 eV for the powder never exposed to IL.

The photocatalytic activity of oxyfluoride NPs was investigated by measuring the evolution of the absorbance spectrum of an aqueous solution of 6.10^5 mol/L of methyl orange dye (MO) as a function of the irradiation time. A 1.6 mg of NPs was placed into the cell containing 3 ml of MO and stirred under darkness for 60 min to establish equilibrium between the dye and the photocatalyst. Then, the solution was placed at a distance of about 20 cm from a 500 W Xenon lamp for irradiation with continuous stirring to have homogeneity between the dye and the catalyst during illumination. The UV–Visible measurements of MO solution were carried out every 20 min up to 120 min. The MO concentration variation (normalized to the initial one), C/C_0, with time can then be plotted since it is equal to the MO absorbance variation, A/A_0, with time. From this, the pseudo-first-order reaction rate of the photocatalyst (k) can be obtained using the Langmuir–Hinshelwood model and by plotting $\ln(A_0/A)$ versus the irradiation time. [32] Hence, the slope of such plot corresponds to k according to equation: $\ln(A_0/A) = kt$ (1)
Where A_0 and A are the absorbance maxima of the MO solution before and after the irradiation time (t in min), respectively.

3. Results and discussions

3.1. NPs synthesis by sputtering in Argon.

First of all, we try to obtain pure Bi metallic NPs in IL by sputtering a Bi target in a pure Ar atmosphere with fixed parameters: a radiofrequency, rf, power of 50 W, an argon flow rate of 30 sccm, equivalent to working pressure (P_w) of $2.3x10^{-2}$ mbar, and a sputtering time of 20 min. After Bi target sputtering in the Ar plasma, the initially transparent IL solution turns to black, which could reveal the presence of metallic Bi NPs. Similarly, Brütsch *et al.* observed a deep black colour when they synthesized Bi nanoparticles into organic solvent by photo-reduction of $BiBr_3$. [33] HR-TEM analysis was performed to confirm this. Figure 1 presents images and the selected-area electron diffraction (SAED) obtained on our suspension. It demonstrates that we synthesized nanometric-sized (typically 5-10 nm) and well crystallized NPs. In average, the diameters of NPs are smaller than 10 nm, which will be confirmed later. NPs shape is isotropic, without any clear faceting. We then assume they are spherical, which could indicate that they are formed

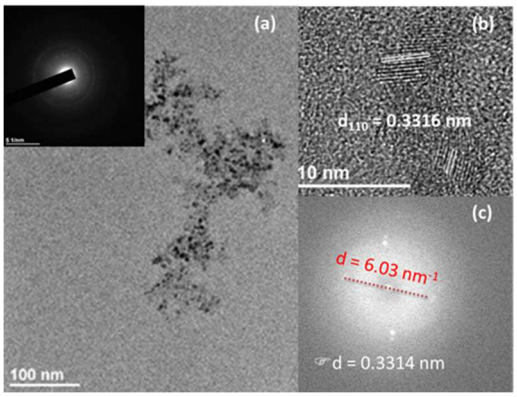

FIGURE 1. (a) General view of nanoparticles obtained by Bi sputtering in IL at P = 50 W, Φ_{Ar} = 30 sccm, and t_s = 20 min. Insert: Experimental SAED pattern of the assembly of nanoparticles. (b) high-resolution TEM image of an individual nanoparticles, interreticular distance about 0.3316 nm is in good concordance with interreticular distance of (110) plane for metallic Bi (c) calculated FFT image of particles shown in (b), interreticular distance is in good agreement with the distance determined in the direct space.

inside the liquid medium and not at the surface, as reported by other authors. [25] The interreticular distance of 0.3316 nm can be assigned to the (110) plane of metallic Bi. [34] EDS spectrum was obtained simultaneously on the NPS in the IL (Figure S.1 in the annex) and confirms that the NPs are made of Bismuth, the other elements are related to IL, which is still present around NPs.

To confirm the NPs nature, larger amounts are synthesized with the same process parameters but with longer time (3 hours). NPs are then extracted from IL and characterized by XRD and XPS. Results are compared to micrometric-size metallic powder. For XRD, this powder was directly analysed; whereas for XPS, it was first dispersed into IL and then extracted thanks to the same protocol than the one used for NPs. The results obtained from XPS and XRD analysis for both Bi NPs and powder are plotted on Figure 2. In XPS, the spectra obtained for Bi 4f is presented on Figure 2a, while the ones for other elements are in supporting information (Figure S2). For NPs and power extracted from IL, the sulphur detection indicates that a thin layer of IL is still present at their surface. From elemental composition, we calculate a S to Bi content ratio of 3 for powder and of 8 from NPs. The higher amount of remaining IL around NPs can be explained by their smaller size, increasing the surface to volume ratio. However, despite this IL layer, we succeed to observe the Bi 4f signal from NPs, which is very close to the one recorded from powder. The main Bi contribution at 159.5 eV corresponds to Bi_2O_3 environment indicating a surface oxidation of the NPs, but a clear contribution at 157.0 eV is also visible, corresponding to metallic Bi. [35] The Figure 2b presents XRD results. The main diffraction peaks observed for NPs are in agreement with the one from powder at 27.3°, 38.0°, 39.7°, 44.6°, 46.1° and 48.7°, corresponding to the planes (012), (104), (110), (015), (006) and (202) respectively of the metallic Bi phase. [36] The very large shoulder of the main peak, marked by an asterisk, could be attributed to the 27.9° peak of the (121) plane in amorphous α-Bi_2O_3, in agreement with XPS results. However, the XRD results confirm that even if the surface of NPs could be slightly oxided, they are unambiguously mainly made of metallic bismuth. Compared to powder, the diffraction peaks of NPs are of course larger due to their smaller size. From Debye Sherrer equation, their coherent domain diameter is estimated to 5 nm, which is coherent with a nanometric size observed by HR-TEM. Finally, we succeed to form by sputtering onto IL NPs of metallic Bismuth.

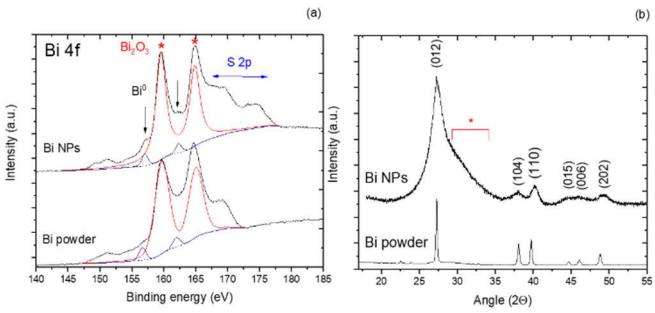

FIGURE 2. (a) Bi 4f spectra from XPS and (b) diffractograms for NPs obtained by sputtering onto IL in pure Argon atmosphere, compared to metallic Bi powder. Plane indexes and arrows refer to Bi phase and * to the α-Bi_2O_3 phase.

After, in order to investigate the influence of plasma parameters, we synthesis Bi NPs with varying rf power (P), argon flow rate (Φ_{Ar}), and sputtering time (t_s), as reported in Table 1. Shorter synthesis times are used here in order to ease the observation of isolated NPs by TEM and not to saturate the UV-visible absorbance measurements of dispersions.

TABLE 1. The deposition parameters used in sputtering bismuth onto [BMIM][TFSI].

P (Watt)	Φ_{Ar} (sccm)	P_w (x10^{-2} mbar)	t_s (min)
50	30	2.3	20
20	30	2.3	20
50	20	1.6	20
50	30	2.3	10

Figure 3 shows the TEM images for various plasma conditions. NPs, with a diameter ranging between 3 and 7 nm (mean diameter ~ 6 nm), were observed without the formation of aggregated secondary particles. The size distribution is coherent with the mean diameter of 5 nm determined from XRD. Comparable sizes ranging from ~ 4 up to ~ 20 nm have also been reported for other metals (Ti, Ag and Au) NPs synthesized in the same IL. [25,37,38] On Figures 3b-d, the diameter does not show any tendency to vary with the power, the argon flow rate, and the deposition time. However, its variation could be lower than the size precision of these measurements (~ 2 nm). Several authors claims that the IL plays a vital role in controlling the size and the stabilization of the growing NPs, more than the plasma parameters. [39] Furthermore, the decrease in the power, the argon flow rate, or the sputtering time seems to result in a reduction of the Bi NPs concentration, probably because of a reduced amount of sputtered Bi atoms reaching the liquid.

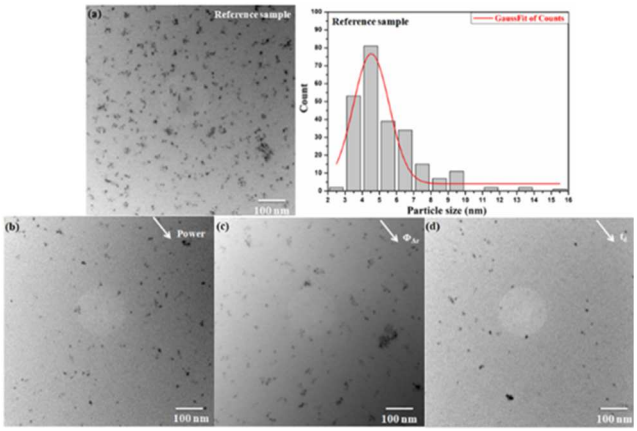

FIGURE 3. TEM images of bismuth nanoparticles sputtered onto IL at (a) P = 50 W, Φ_{Ar} = 30 sccm, t_s = 20 min (reference sample) and size distribution associated, (b) P = 20 W, Φ_{Ar} = 30 sccm, t_s = 20 min, (c) P = 50 W, Φ_{Ar} = 20 sccm, t_s = 20 min, and (d) P = 50 W, Φ_{Ar}= 30 sccm, t_s = 10 min and the histogram corresponding to the reference sample.

The UV-visible absorption spectra of Bi NPs in IL were measured and their Δ(absorbance) are shown in Figure 4a, using initial IL as background. First, we observe the variation of the baseline in the 400-900 nm wavelength region. Since metals absorb in the visible range, the presence of metallic NPs can explain this baseline variation. The more intense baseline in the case of a plasma at P = 50 W, Φ_{Ar} = 30 sccm, and t_s = 20 min indicates the presence of a higher NP concentration in this condition. The decrease in the power, the sputtering time, or the argon flow rate results in a reduction of NPs concentration, and so, in the baseline of the UV-visible absorption spectra, in agreement with TEM images (Figure 3). Second, we might remark, in all spectra, that two peaks appear at 245 and 296 nm. Many authors use UV-visible spectra to detect the presence of metallic NPs by taking advantage of their specific absorption by plasmon resonance. Gutiérrez et al. found out that nanometer-sized bismuth particles exhibited absorption at ~253 nm. [40] Besides, Creighton et al. declared that the first absorption band of 10 nm bismuth particles should appear around 270-280 nm. [41] Additionally, Fang et al. demonstrated that the absorption peak of the ~20 nm aqueous bismuth nanoparticle colloids is centered at ~268 nm. [42] However, these peaks could also come from interaction between IL and NPs or to an IL modification due to the plasma exposure. To investigate this latter hypothesis, we try to submit IL to an Ar plasma, without NPs formation.

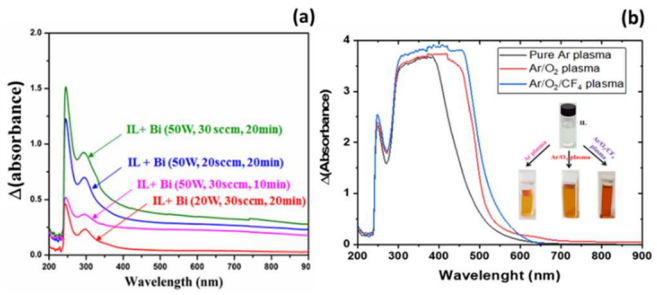

FIGURE 4. Spectra of Δ(Absorbance) = Absorbance(after exposure) - Absorbance(initial IL) of (a) bismuth NPs obtained in IL after sputtering in pure Ar plasma under different conditions of power, argon flow rate, and sputtering time, and (b) IL after MW plasma exposure for 1 hour in Ar (black), Ar/O_2 29:1 (red), and $Ar/O_2/CF_4$ 29:0.3:0.7 (blue).

For this purpose, we exposed the [BMIM][TFSI] IL to an Ar microwave plasma. In order to enhance the potential impacts, the plasma exposure lasted for 1 hour (much higher than for NPs synthesis fixed at 20 min). Moreover, we might notice that the microwave plasma used in this part is different from the radiofrequency one used after for NPs formation. More specifically, it is known to possess higher electronic density, hence potentially higher density of ions and of reactive radicals available to interact with the IL. This will enhance their effect on IL. At first, visual observations show that IL changed from transparent to orange after the interaction with Ar plasma, as it can be seen in enclosed pictures of the Figure 4b. The UV-visible absorption of IL before and after exposure is recorded and plotted in Figure S.3.a in supplementary information. The initial IL spectrum presents two absorption peaks at around 220 and 270 nm. After plasma exposure, these peaks increase in absorbance and enlarge to higher wavelengths. To highlight the modifications induced by the plasma, these spectra are plotted in Figure 4b considering the spectrum of initial IL as the blank. In the case of Ar plasma, two peaks appeared: one around 250 nm and a second broad one from 300 to 450 nm. During IL/ plasma interaction, many phenomena may explain these changes: a temperature increases of the IL, the impact of charged species like electrons and ions or the expose to plasma UV-visible light. The presence of broad peaks on UV-visible spectra and a change in IL colour were also reported after exposure of different ILs to surface wave. [43,44] These alterations were mainly attributed to the ionic bombardment, and in smaller proportion to the plasma light exposure. In our case, it seems that these both factors can play a role. In the case of Bi NPs formation (Figure 4a), the peaks observed in the 200-450 nm wavelength region could also be linked to this IL modification by the plasma, hiding any potential smaller peak due to plasmon absorption of Bi NPs.

Finally, we succeeded for the first time in synthesizing Bi NPs by sputtering a Bi target on an IL in pure Ar atmosphere. We also showed that the baseline in visible region of UV-visible spectra is a good indication of the metallic NPs presence, whereas peaks at low wavelengths are attributed to IL modification by the plasma. To go further, we will now try to form NPs of Bismuth oxyfluoride compound by adding O_2 and CF_4 to the Ar plasma.

3.2. NPs synthesis by reactive sputtering in $Ar/O_2/CF_4$

3.2.1. IL modification by $Ar/O_2/CF_4$ plasma. Before the NPs synthesis, since we just showed, that plasma exposure induces changes in IL, we will first investigate the effect of O_2 and CF_4 addition on these modifications, without NPs formation. On Figure 4b, the Δ(absorbance) of IL after exposure to Ar/O_2 29:1 and $Ar/O_2/CF_4$ 29:0.3:0.7 plasmas are added. When O_2 was introduced, the second peak at 270 nm, already observed after exposure to pure Ar plasma, became broader, while the injection of CF_4 enlarged the peak width to a greater extent and the intensity of the orange colour increased. These results shows that the reactive gases addition enhances the IL modification by the plasma.

In order to estimate the part of modified IL, IR spectroscopy was used to analyse it after $Ar/O_2/CF_4$ 29:0.3:0.7 plasma treatment, where the modifications are observed to be the highest. Figure 5a and b presents the transmission and ATR IR spectra of IL and the subtracted spectrum, to highlight the plasma modification. The main discrepancy is the presence the two bands at 3560 and 3640 cm^{-1} in Figure 5a that correspond to the vibration bands of the water molecule in the ionic liquid. [45] The spectra difference is then mainly due to different water sorption in the samples, probably during storage. Moreover, the bands between 2750 and 3300 cm^{-1} are assigned to the CH stretching vibration bands of the imidazolium cation but the difference of the CH bands is very low (around 1 %). Similarly, the possible degradation of the anion was estimated by ATR, as shown in Figure 5b. The changes

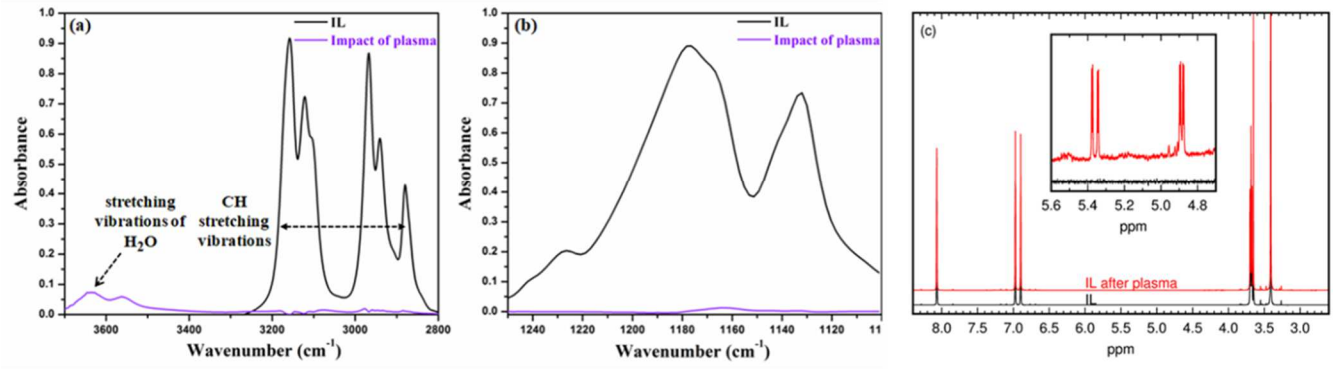

FIGURE 5. (a) Transmission IR, (b) ATR-IR spectra for initial and the spectra difference between before and after exposure to an $Ar/O_2/CF_4$ 29:0.3:0.7 plasma, and (c) ^1H RMN spectra of IL before and after plasma exposure. The insert figure is a zoom on new peaks related to aromatic ring.

are also small (around 1%) for anion vibrations. Neither the anion nor the cation has been substantially modified and no conjugated carbon was detected. Therefore, the impact of plasma should be relatively small. Hence, despite the impressive change of coloration of the IL, IR spectroscopy indicated that the degradation of the IL is relatively modest, evaluated below 1% of degradation after 1 hour.

To confirm this limited impact on IL in plasma conditions closer to the NPs deposition one, we investigated by NMR the IL supernatant that have undergone $Ar/O_2/CF_4$ radiofrequency sputtering process. Obtained ^{13}C, ^{15}N and ^{19}F spectra (on Figure S.3b in the annex) show no difference compared to initial ionic liquid. Although, on ^1H spectra, which is the most sensitive nucleus, plotted on Figure 5c, we can observe some new peaks on spectra after process related to the aromatic ring (insert Figure). This part of the cation is a chromophore, its modification is then coherent with a strong change of the UV-visible spectrum and of IL colour. However, this peak maximum intensity does not exceed 0.4 % of the original signal.

Finally, in this first section, we showed that plasma by itself modifies the IL. This modification seems to be due to ions and/or plasma light in Ar atmosphere, but also depends on reactive species when O_2 and CF_4 are added. We may notice that this effect is visible by a drastic peak shift in the 200-450 nm wavelength region on UV-visible absorption spectra but corresponds to IL degradation lower than 1% after 1 hour of exposition to the plasma.

3.2.2. Synthesis of Bi-based compounds NP by reactive sputtering. In a second step, we try to deposit NPs of Bismuth oxyfluoride by adding reactive gases during sputtering, keeping all the other parameters identical (P = 50 W, t_s = 20 min, and a total gas flow rate of 30 sccm). The target was sputtered with different O_2 and CF_4 flow rates, Φ_{O2} and Φ_{CF4}, reported in Table 2. Again, before each experiment, the same protocol was applied: the target cleaning in pure argon, the $Ar/O_2/CF_4$ gas mixture injection and its stabilization before starting the NPs synthesis.

TABLE 2. Synthesis of NPs in [BMIM][TFSI] with various Φ_{O2} and Φ_{CF4}.

Φ_{O2} (sccm)	0.3	0.5	0.8
Φ_{CF4} (sccm)	0.7	0.5	0.2

Figure 6a-c shows TEM images and the corresponding histograms of the NPs size distributions obtained at different Φ_{O2} and Φ_{CF4}. The images indicate that NPs are formed in all cases, even if they seem to be more aggregated than for Bi NPs. The mean diameter of most particles is determined to be less than 10 nm. However, it is difficult to claim a significant difference in size between particles obtained at different reactive flow rates at this stage.

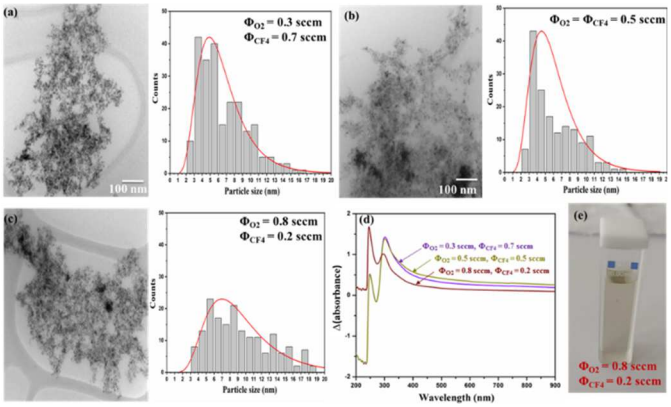

FIGURE 6. TEM images (left) and size histograms (right) of NPs in IL obtained at (a) Φ_{O2} = 0.3 and Φ_{CF4} = 0.7 sccm, (b) Φ_{O2} = Φ_{CF4} = 0.5 sccm, and (c) Φ_{O2} = 0.8 and Φ_{CF4} = 0.2 sccm; (d) Δ(absorbance) spectra at the same conditions and, (e) picture of dispersion obtained at Φ_{O2} = 0.8 and Φ_{CF4} = 0.2 sccm.

The optical absorption spectra of the various suspensions obtained are displayed in Figure 6d. In the 200-400 nm region negative values appear due to background correction with the utilization of the initial IL spectrum and because this region is very sensible to peaks shift due to IL modification by plasma. The directly measured UV-visible spectra are plotted in Figure S.4 in supporting information. Again, the region from 200 to 350 nm relies to this IL modification by plasma. In 400-900 nm, the non-null baseline could indicate that metallic NPs are present in suspension. This baseline decreases for O_2/CF_4 0.8:0.2 sccm and

the solution becomes transparent (Figure 6e), while NPs are still observed by TEM. This could indicate the presence of non-metallic NPs. The HRTEM images and FFT analyses of NPs obtained with this latter gas mixture are presented in Figure 7. The results clearly show that the NPs are well crystallized and with isotropic shape. Again, few NPs present an interreticular distance of approximately 0.3304 nm assigned to (110) plane of Bi phase; but an interreticular distance of ~0.3455 nm is also observed for other particles. This distance can be attributed neither to Bi nor to Bi_2O_3. [33] This distance could be compatible with the interreticular distances of the (111) planes of the fluorinated phases, $BiO_{0.5}F_2$ (JCPDS 24-0147), the phase observed in case of thin films deposition, but is also compatible with $Bi_7O_5F_{11}$ (JCPDS 50-0003) or BiF_3 (in cubic (JCPDS 51-0944) or orthorhombic (JCPDS 70-2407) phases) without being able to specifically distinguish them. On the other hand, the BiOF (JCPDS 73-1595) phase does not seem to be obtained, the position of its most intense peak corresponding to smaller interreticular distances. Indeed, even though the exact nature of this phase cannot be clearly identified, the HR-TEM images evidence that the addition of O_2 and CF_4 gases in the plasma leads to the formation of an original class of NPs in the IL. However, for all the reactive gas mixtures, the dispersions contain this oxyfluoride in mixture with metallic NPs. This result can be compared to what it is observed in case of thin film deposition. [46] In this latter case, with all process parameters identical, films are a mixture of Bi and oxyfluorinated domains for $\Phi_{O2} \leq 0.5$, while they are pure oxyfluorides for $\Phi_{O2} \geq 0.6$ (see Figure S.5 in supporting information). Hence, the equilibrium of sputtered and reactive species that controlled the nature of formed compound seems to be different between thin film and NP synthesis.

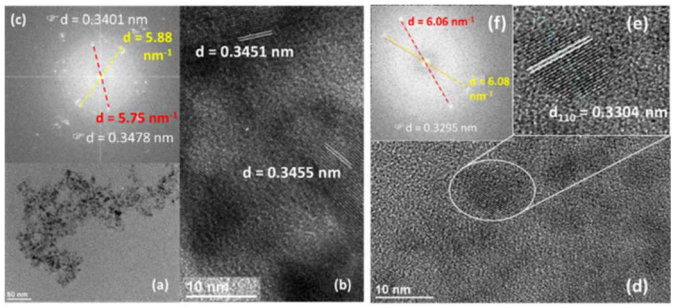

FIGURE 7. TEM image of (a) selected NPs after sputtering Bi with $\Phi_{O2} = 0.8$ and $\Phi_{CF4} = 0.2$ sccm. (b) Zoom on individual NP. Interreticular distance about 0.3450 nm are found. Such interreticular distances are not compatible with Bi and Bi_2O_3. (c) Calculated FFT pattern of image (b), determined distances are in good concordances with the ones obtained in the direct space. (d) individual NP (e) zoom, the interreticular distance about 0.3304 nm can be assigned to the (110) plane of Bi. (f) Calculated FFT pattern of image (e), with concordant interreticular distance.

Similarly to metallic Bi NPs and in order to clarify the exact nature of oxyfluoride NPs, higher amount of pure compound is formed using longer deposition time (3 hours) and higher reactive gas flow rates but keeping the same O_2 to CF_4 ratio than O_2/CF_4 0.3:0.7. The obtained NPs are then extracted and analysed by XPS and XRD, as previously. Again, results are compared to compound in powder, presenting micrometric size. In that case, powder where directly analysed by XPS and XRD, without experiencing dispersion into IL.

The comparison between NPs and reference powder by XPS on Figure 8a-c confirms that the NPs synthesized are Bismuth oxyfluoride. Their XPS peaks position corresponds to $BiO_{0.5}F_2$ compound: Bi^{3+} at 159.9 eV, O-Bi at 530.5 eV and F-Bi at 684.4 eV. [35] Based on these Bi, O and F contribution, we determined a O/Bi ratio of 0.4 and a F/Bi one of 0.9, which are not exactly the one expected for $BiO_{0.5}F_2$ phase. This indicates that these contributions come from NPs "bulk" composition but also from bonds at their interface, especially with IL. Indeed, like for metallic NPs, contributions from IL can also be seen: S=O from S 2p signal at 168.5 eV, O-S from O 1s signal at 532.4 eV and F-C from F 1s signal at 688.8 eV. [47] Hence, the oxyfluoride NPs also possess a thin layer of IL at their surface. However, their S to O content ratio (= 0.4) is significantly lower than in case of metallic NPs (= 8), indicating a lower amount of remaining IL. This is confirmed by the lower S 2p signal for these NPs (Figure 8a) compared to the one observed for metallic NPs (Figure 2a). This lower amount of IL on the oxyfluorides could be due to a

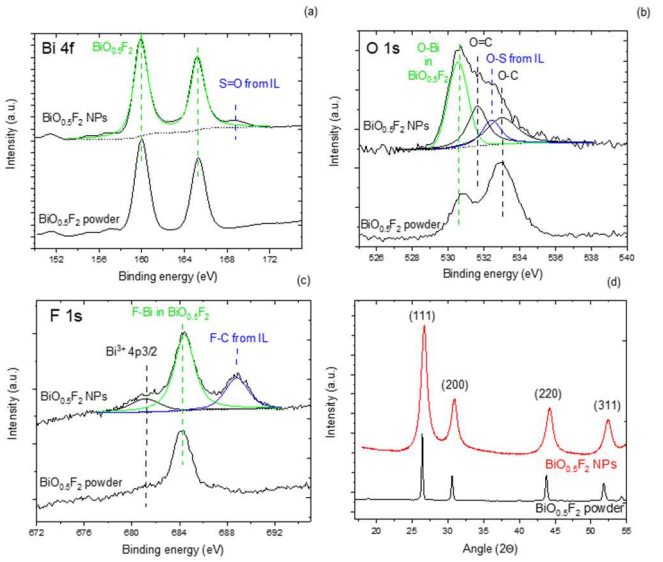

FIGURE 8. XPS spectra for (a) Bi 4f and S 2p, (b) O 1s and (c) F 1s and (d) diffractogram for NPs obtained by sputtering onto IL in $Ar/O_2/CF_4$ 28:0.6:1.4 atmosphere compared to $BiO_{0.5}F_2$ powder.

lower affinity between this compound and the IL. Hence, the IL is less efficient to separate NPs, which could explain why these oxyfluoride NPs are observed to be more agglomerated by TEM (Figure 6) than the metallic ones. The XRD analysis of NPs, plotted in Figure 8d, confirms the $BiO_{0.5}F_2$ phase with the presence of peaks at 26.7°, 30.9°, 44.3° and 52.5° corresponding to the (111), (200), (220) and (311) planes of this phase. Again, the diffraction peaks are larger for NPs than for powder, because of the size difference. The NPs mean diameter is estimated to 7-8 nm, again in agreement with the size distribution determined by TEM (Figure 6). Since mean diameter values are very close for the four XRD peak, this confirm the spherical shape of the $BiO_{0.5}F_2$ NPs.

Finally, it is important to point out that since no further fluorination can occur when sample are out of the reactor, this oxyfluoride compound is formed during plasma process. Moreover, we might notice that no fluoride or oxyfluoride compound was observed in previous case, in pure Ar atmosphere. The fluorination of NPs occurs then thanks to reactions with species from plasma and not with fluorinated part of IL. Indeed, we succeed for the first time to form in one step NPs of compound by controlling a reactive atmosphere during the sputtering onto IL.

To illustrate the interest of such synthesis for photocatalytic applications, we then tested $BiO_{0.5}F_2$ NPs for degradation of methyl-orange under UV-Visible irradiation.

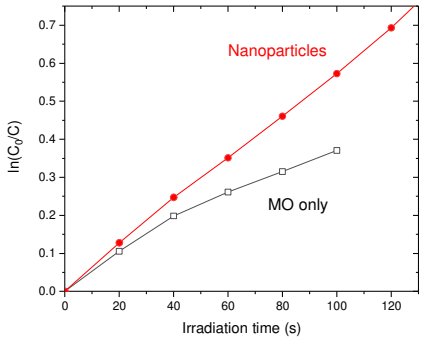

FIGURE 9. $Ln(C_0/C)$ as function of irradiation time for photodegradation of methyl-orange into water under illumination with (full symbols) and without (open symbols) $BiO_{0.5}F_2$ nanoparticles.

The Figure 9 shows the degradation of MO dye, ln (C_0/C), as a function of the irradiation time with and without presence of Bismuth oxyfluoride in NP. It confirms that these nanoparticles present a photocatalytic activity to degrade MO under illumination. The linear behaviour observed for NPs seems to indicate a reaction kinetics of the first order. Indeed, we succeed by the reactive sputtering onto ionic liquid method to synthesize original photocatalyst at nanometric size. These compounds could also be tested for other applications. For instance, they could be interesting as positive electrodes in Lithium batteries [35,49,49], to take advantages of their small size to enhance the specific surface area, or in batteries using IL as electrolyte [50], since they are already in contact with it. Moreover, since this synthesis method is general, it could be applied to other compounds, obtained usually in thin films by reactive sputtering.

3.3. Mechanisms for reactive sputtering onto IL

The formation of nanoparticles by sputtering onto liquid is not yet completely understood. Hence, the places where occur the different steps of NPs formation are not well elucidated. Wender *et al*. proposed three different possible mechanisms for the formation of sputtered gold NPs: with nucleation step occurring at the surface of IL and the NP growth in the IL volume (I), with both nucleation and growth steps at the surface (II) or with both steps in the volume (III). [39] Those different mechanisms might be obtained depending on various process parameters like the energy of impinging sputtered species, the viscosity and the temperature of IL, the surface coordination ability depending on material and IL affinity, etc. In our case, the NPs formed in all gas mixture conditions are isotropic, which indicate a good solvation of Bi-based materials into [BMIM][TFSI] avoiding a film formation on its top. Hence, the NPs growth seems to occur inside the solution as reported for silver [25], that is to say following the model (I) or (III) proposed by Wender *et al*.

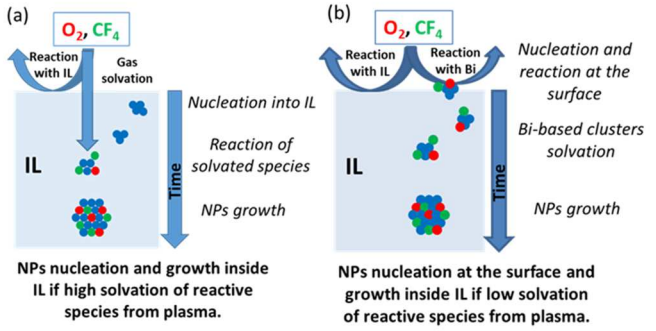

FIGURE 10. Schematic mechanisms for reactive sputtering of Bi target in $Ar/O_2/CF_4$ atmosphere onto IL (a) considering high and (b) low solvation of reactive species from plasma.

In reactive mode, a second question emerges to find out the mechanism of NPs formation: Where do the oxidation and fluorination reactions take place? Many authors reported the formation of oxide NPs by reaction with air after the synthesis of metallic NPs. [51] This observation proves that some oxidized species, most probably water from air, might be solvated into IL after process and then react and modify the NPs. However, in the present paper, the formation of oxyfluorinated compound in O_2/CF_4 mixtures cannot be explained by post-synthesis reactions and so might take place during the plasma process. If the nucleation step occurs in the IL volume, to form Bi-based compounds, reactive species from the plasma should be solvated into the liquid, as shown in Figure 10a. However, oxygen is a non-polar gas and has very low solubility and weak interactions with ionic liquids, including [BMIM][TFSI]. [43,52] The measurements of O_2 in [BMIM][TFSI] were determined by Bahadur et al., where O_2 has a solubility of 0.15 mole fraction at 500 mbar and 303 K. [45] The amount of dissolved O_2 in our IL phase was calculated around 6.10^{-6} mole fraction. Because of their high reactivity, we might assume that solvated radicals like O or F will quickly react with IL as the major phase. Their diffusion length inside IL should then be very limited and their probability to modify NPs also. This is then reasonable to think, that reactive species from plasma will mainly and more efficiently react with Bi clusters at the top surface of IL or very close to its subsurface during the nucleation step (see the Figure 10b). Moreover, we might also notice that in all TEM images, core/shell structure has never been observed. This agrees with the direct creation of Bi-O and Bi-F bonds during the NPs

formation rather than an oxidation/ fluorination of an already formed NPs. The Bi-O and Bi-F bonds should then be formed at the first stage of clusters formation and their aggregation conducts to the NPs growth.

In order to confirm this hypothesis, we exposed a metallic Bismuth thin film directly to an Ar/CF_4 plasma and indirectly, putting it at a bottom of a Petri dish filled by IL. The Figure 11a presents the XRD pattern of the film before and after indirect plasma exposure during one hour. Thanks to the presence of IL between plasma and sample (whose thickness is estimated to be 1.5 mm) the film structure is totally unchanged; contrary to the one directly exposed to plasma (XRD patterns in Figure S6 in supporting information). Hence, the fluorination of the metallic bismuth is not possible through the IL. During NPs synthesis, their fluorination and their oxidation should happen when they are close the IL top surface, as represented on Figure 10b.

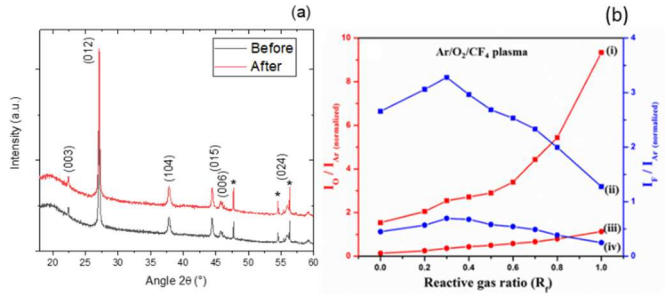

Figure 11. (a) XRD patterns for Bi metallic film before and after 1h exposure to MW Ar/CF_4 plasma. Plane indexes refer to Bi phase planes and * to the Silicon substrate. (b) I_O/I_{Ar} (red) and I_F/I_{Ar} (blue) in the $Ar/O_2/CF_4$ plasma as a function of the reactive gas ratio ($R_f = \Phi_{O2}/ (\Phi_{O2}+ \Phi_{CF4})$) in the absence (i, ii) and presence (iii, iv) of [BMIM][TFSI].

If we assume the Bi-O and Bi-F bands are formed on the top of IL surface, the mechanisms that control the nature of NPs could seem to be close to those happening during thin film growth. However, we already highlight in section 3.2.2., the difference between both process: for high Φ_{O2} (≥ 0.6), pure bismuth oxyfluoride thin films are obtained without any metallic Bi domains [46], whereas metallic NPs are still present in the same condition. Since the flux of sputtered bismuth atoms from the target and the injected reactive gas flow rates were the same, phenomenon should explain this discrepancy. One explanation could be linked to a rapid solvation of Bi clusters, which will limit their presence time at the surface, and then protect them from being oxided and/ or fluorinated. However, we may also wonder if the presence of IL could have an influence on the plasma by itself.

Indeed, to investigate this hypothesis, we analyse plasma with various $Ar/O_2/CF_4$ mixtures by Optical Emission Spectroscopy (OES). In order to avoid the reactive gases consumption by getter effect, that is to say by the sputtered Bi atoms, we performed this analysis in microwave plasma. We more particularly follow the normalized intensity of O* (I_O/I_{Ar}) at 844.6 nm and F* lines (I_F/I_{Ar}) at 703.7 nm to the Ar* one at 696 nm in presence and in absence of IL in the reactor. The Figure 11b shows the variation of the O and F radicals signals for various gas mixture with and without IL. When we go from CF_4-rich to O_2-rich gas mixture, the intensity of O line increases while that of F decreases in both cases, as expected. However, for similar amounts of injected gases, the intensities of O and F lines in the presence of IL is drastically lower (by more than 50 %) than without IL. At low pressure, the density of such radicals is controlled by a balance between their formation in the plasma volume (by dissociation of O_2 and CF_4 molecules from electronic impact) and their loss by reactions with reactor surfaces. Since here, the plasma conditions are unchanged, the signal decrease could be interpreted as an increase of radical loss in presence of IL. In the liquid phase, this loss could be due to surface reactions or to gas solubilization into the liquid. We previously calculated that the amount of dissolved O_2 in our IL phase is around 2.10^{-7} mole fraction, very low compared to the amount injected during one hour. We may assume that solubility of reactive oxidized or fluorinated radicals in IL is not higher. Such a small amount is an indication that neutral species from plasma are not mainly lost by gas absorption but by reaction on IL surface with a higher loss coefficient than on solid surface. Indeed, contrary to a solid surface with a limited number of reaction sites, which could be saturated by reactions with radicals, the surface of a liquid may be refreshed by inner convection movement that will increase the radical loss probability. Hence, even with the same injected reactive gas flow rate, the presence of IL decreases the density of radical species available to react with the sputtered Bi atoms, which leads to keep some metallic domains compared to thin film deposition.

Finally, the presence of metallic NPs in mixture with oxyfluoride NPs in case of sputtering onto IL, compared to fully oxyfluorinated thin films obtained in the same atmosphere, can be explained by two phenomena: i) a rapid solvation of Bi-based clusters might reduce their presence time on the IL surface, where they are efficiently in contact with reactive species, and ii) the fluxes of reactive species available to react with Bi clusters are also reduced because these species are demonstrated to react with the IL itself. The overall mechanisms occurring during reactive sputtering and controlling the NPs nature are then summarized in the Figure 10b. In this paper, the particularly investigate the influence of reactive gas flow rate on formed NPs nature. However, many authors report the influence of IL nature, especially its surface tension and its viscosity, on the solvation time of clusters. [54] To go further on the mechanism in reactive mode, it could be very interesting now to compare the nature of NPs formed with a fixed reactive gas mixture using various ILs.

Conclusions

First, we studied the non-reactive sputtering of a Bi target onto [BMIM][TFSI] IL, which to our knowledge was never done. In pure Ar plasma, isotropic, crystallized and well-dispersed metallic bismuth NPs have been generated. Their size ranges between 3-7 nm. The variation of the sputtering parameters

such as the power, argon flow rate, and sputtering time seems to influence their concentration without significantly affecting their size.

In a second step and for the first time, the reactive mode was applied to the sputtering onto IL technique. We succeeded in synthesizing spherical and crystallized $BiO_{0.5}F_2$ NPs with a size distribution ranging between 3 and 10 nm in $Ar/O_2/CF_4$ atmosphere. Depending on the O_2 and CF_4 reactive gases flow rates, these Bismuth oxyfluoride NPs could be in mixture with metallic ones. We demonstrate that radicals from the plasma do not modify compounds into ionic liquid and so, that reaction between sputtered Bi atoms and radicals occurs at liquid top surface (or very close to its subsurface). We explained the presence of metallic NPs by a higher consumption of O and F radicals from plasma by the presence of IL leading to lower radical densities available to react with sputtered Bi atoms. To explain our results, we propose a mechanism based on reactions of species from plasma with Bi clusters at the IL surface. The content of compound NPs versus metallic ones is then the result of the equilibrium between the sputtered Bi flux from the target and the reactive gas flow rates, similarly to thin film deposition, but also by the time for cluster solvation into the IL volume and by the reactive species consumption by the IL itself. Since the main reactions for the compound NPs formation occur at the IL surface, they should be influenced by the nature of arriving species (atom or nuclei). Here, we used a relatively high pressure which could lead to Bi nuclei formation into the gas phase. It could be very interesting to investigate synthesis at lower pressure, where this nuclei formation in gas phase is limited. Moreover, since the solvation time of clusters seems to influence the nature of NPs, it could be very interesting to investigate the composition of NPs obtained with the same reactive gas mixture but with different ILs.

Furthermore, these original results demonstrate that reactive sputtering onto an IL is an efficient and promising method for synthesizing Bi-based compound in NPs, with a diameter lower than 10 nm and with a relatively sharp size distribution. An example application is presented: the MO photodegradation acceleration in presence of bismuth oxyfluoride NP highlights the interest of such method to obtain original photocatalyst with nanometric size. These compounds could also be tested for other applications. They could be particularly interesting as positive electrode for lithium batteries or those using IL as electrolyte. Indeed, we could take advantage of the small NPs size to enhance the specific surface area and to their direct synthesis into IL. Moreover, since this synthesis is a general method, it could be applied to other target and reactive gases in order to form NPs of a large variety of compounds, usually obtained in thin films by reactive sputtering.

Conflicts of interest

There are no conflicts to declare.

Acknowledgements

The authors would like to thank Christophe Caperaa for his contribution on some synthesis experiments. The authors also thank the platform Centre Imagerie Cellulaire Sante (Clermont Auvergne University), most notably Christelle Blavignac, for her technical assistance in TEM analysis (Hitachi H7650) and Armel Descamps-Mandine from Centre de Microcaractérisation Raimond Castaing (UMS3623) for HRTEM analysis and fruitful discussions about HRTEM results. The authors acknowledge the support received from the Agence Nationale de la Recherche of the French government through the program "Investissements d'Avenir" (Grant No. 16-IDEX-0001 CAP 20-25).

Supporting information

Additional supporting information is available in the online version of this article at the publisher's website or from the author.

- Protocols for TEM grid preparation and NPs extraction from IL
- Figure S1: EDS spectrum obtained on the NPS sputtered with Ar plasma onto the IL.
- Figure S2: C 1s and O 1s XPS spectra for NPs produced in pure Ar plasma compared to metallic powder.
- Figure S3: Measured UV-visible spectra (a) for IL before and after exposure to Ar, Ar/O_2 and $Ar/O_2/CF_4$ plasmas and (b) ^3C and (c) ^{19}F NMR spectra of IL before and after plasma treatment in $Ar/O_2/CF_4$.
- Figure S4: Measured UV-visible spectra for IL before and after sputtering in various $Ar/O_2/CF_4$ plasma mixtures.
- Figure S5: XRD patterns of metallic Bismuth thin film before and after its direct exposure for one hour to a Ar/CF_4 MW plasma.

Notes and references

1 H. Wender, P. Migowski, A.F. Feil, S.R. Teixeira, J. Dupont, *Coordination Chemistry Reviews*, 2013, **257**, 2468.
2 S.K. Pradhan, P.J. Reucroft, F. Yang, A. Dozier, *Journal of Crystal Growth*, 2003, **256**, 83.
3 S.-J. Candace Tsai, M. Hofmann, M. Hallock, E. Ada, J. Kong, M. Ellenbecker, *Environ. Sci. Technol.*, 2009, **43**, 6017.
4 D.S. Choi, A.W. Robertson, J.H. Warner, S.O. Kim, H. Kim, *Advanced Materials*, 2016, **28**, 7115.
5 D.D. Vaughn, J.F. Bondi, R.E. Schaak, *Chemistry of Materials*, 2010, **22**, 6103.
6 D. Yang, C. Li, G. Li, M. Shang, X. Kang, J. Lin, *Journal of Materials Chemistry*, 2011, **21**, 5923.
7 P. Yang, J. Zheng, Y. Xu, Q. Zhang, L. Jiang, *Advanced Materials*, 2016, **28**, 10508.
8 H. Wender, L.F. de Oliveira, A.F. Feil, E. Lissner, P. Migowski, M.R. Meneghetti, S.R. Teixeira, J. Dupont, *Chemical Communications*, 2010, **46**, 7019.
9 Y. Ishida, S. Udagawa, T. Yonezawa, *Colloids and Surfaces A: Physicochemical and Engineering Aspects*., 2016, **498**, 106.
10 E. Ahmed, J. Breternitz, M.F. Groh, M. Ruck, *Cryst Eng Comm*., 2012, **14**, 4874.
11 Z. He, P. Alexandridis, *Phys. Chem. Chem. Phys*., 2015, **17**, 18238.
12 T. Torimoto, K. Okazaki, T. Kiyama, K. Hirahara, N. Tanaka, S. Kuwabata, *Applied Physics Letters*, 2006, **89**, 243117.

13 C. Janiak, Metal nanoparticle synthesis in ionic liquids, in: Ionic Liquids (ILs) in *Organometallic Catalysis*, Springer, 2013, **17**.
14 G. Ye, Q. Zhang, C. Feng, H. Ge, Z. Jiao, *Physical Review B*, 1996, **54**, 14754.
15 M. Wagener, B. Günther, *Journal of Magnetism and Magnetic Materials*, 1999, **201**, 41.
16 M.T. Nguyen, T. Yonezawa, *Science and Technology of Advanced Materials*, 2018, **19**, 883.
17 S.C. Hamm, R. Shankaran, V. Korampally, S. Bok, S. Praharaj, G.A. Baker, J.D. Robertson, B.D. Lee, S. Sengupta, K. Gangopadhyay, *ACS Applied Materials & Interfaces*, 2012, **4**, 178.
18 Y. Oda, K. Hirano, K. Yoshii, S. Kuwabata, T. Torimoto, M. Miura, *Chemistry Letters*, 2010, **39**, 1069.
19 K. Yoshii, K. Yamaji, T. Tsuda, H. Matsumoto, T. Sato, R. Izumi, T. Torimoto, S. Kuwabata, *Journal of Materials Chemistry A*, 2016, **4**, 12152.
20 F. Dong, T. Xiong, Y. Sun, Z. Zhao, Y. Zhou, X. Feng, Z. Wu, *Chemical Communications*, 2014, **50**, 10386
21 Y. Sun, Z. Zhao, W. Zhang, C. Gao, Y. Zhang, F. Dong, *Journal of Colloid and Interface Science*., 2017, **485**, 1.
22 Y. Zhou, W. Li, Q. Zhang, S. Yan, Y. Cao, F. Dong, F. Wang, *Phys. Chem. Chem. Phys*., 2017, **19**, 25610.
23 S. Ibrahim, P. Bonnet, M. Sarakha, C. Caperaa, G. Monier, A. Bousquet, *Materials Chemistry and Physics*, 2020, **243**, 122580.
24 S. Zou, F. Teng, C. Chang, Z. Liu, S. Wang, *RSC Adv*., 2015, **5**, 88936.
25 X. Carette, B. Debièvre, D. Cornil, J. Cornil, P. Leclère, B. Maes, N. Gautier, E. Gautron, A.-A. El Mel, J.-M. Raquez, S. Konstantinidis, *J. Phys. Chem. C*, 2018, **122**, 26605.
26 Kazutaka Akiyoshi, Tatsuya Kameyama, Takahisa Yamamoto, Susumu Kuwabata, Tetsu Tatsuma and Tsukasa Torimoto, *RSC Advances*, 2020, **48**, 28516.
27 M. Porta, M. Thanh Nguyen, T. Yonezawa, T. Tokunaga, Y. Ishida, H. Tsukamoto, Y. Shishino and Y. Hatakeyama, *New J. Chem*., 2016, **40**, 9337.
28 M. Meischein, X. Wang, A. Ludwig, *J. Phys. Chem. C*, 2021, **125**, 24229.
29 M. Ahrenberg, M. Beck, C. Neise, O. Keßler, U. Kragl, S.P. Verevkin, C. Schick, *Physical Chemistry Chemical Physics*, 2016, **18**, 21381.
30 D. Ma, Y. Zhao, J. Zhao, Y. Li, Y. Lu, D. Zhao, *Superlattices and Microstructures*, 2015, **83**, 411-421.
31 M. Ren, F. Teng, Y. Yang, Y. Zhai, W. Gu, Z. Liu, Z. Liu, Y. Teng, *Materials and Design*, 2017, **131**, 402-409.
32 M.A. Rauf, S.S. Ashraf, *Chem. Eng. J.,* 2009, **151**, 10–18.
33 L. Brütsch, C. Feldmann, *Zeitschrift Für Anorganische Und Allgemeine Chemie*, 2017, **643**, 2045.
34 M. Bervas, L. C. Klein and G. G. Amatucci, *J. Electrochem. Soc.,* 2006*,* **153***,* A159.
35 A.J. Gmitter, A. Halajko, P.J. Sideris, S.G. Greenbaum, G.G. Amatucci, *Electrochimica Acta*, 2013, **88**, 735-744.
36 Y. Zhao, Z. Zhang, H. Dang, *Materials Letters*, 2004, **58**, 790-793
37 Y. Hatakeyama, S. Takahashi, K. Nishikawa, *J. Phys. Chem. C*, 2010, **114**, 11098.
38 D. König, K. Richter, A. Siegel, A. Mudring, A. Ludwig, *Advanced Functional Materials*, 2014, **24**, 2049.
39 H. Wender, L.F. de Oliveira, P. Migowski, A.F. Feil, E. Lissner, M.H.G. Prechtl, S.R. Teixeira, J. Dupont, *J. Phys. Chem. C*, 2010, **114**, 11764.
40 M. Gutiérrez, A. Henglein, *The Journal of Physical Chemistry*, 1996, **100**, 7656.
41 J.A. Creighton, D.G. Eadon, *Faraday Transactions*, 1991, **87**, 3881.
42 J. Fang, K.L. Stokes, J.A. Wiemann, W.L. Zhou, J. Dai, F. Chen, C.J. O'Connor, *Materials Science and Engineering: B*, 2001, **83**, 254.
43 H. Himura, A. Irie, S. Masamune, *Transac. Mater. Research Soc. Japan*, 2011, **36**(1), 59.
44 M. Miyagishi, A. Irie, H. Himura, S. Masamune, A. Sanpei, N. Hasuike, N. Ichinose, T. Wakasugi, *J. Plasma Fusion Res.*, 2009, **8**, 608.
45 I. Bahadur, K. Osman, C. Coquelet, P. Naidoo, D. Ramjugernath, *The Journal of Physical Chemistry B*, 2015, **119**, 1503.
46 S. Ibrahim, PhD, Clermont Auvergne University, 2020.
47 O. Höfft, S. Bahr, M. Himmerlich, S. Krischok, J. A. Schaefer, and V. Kempter, *Langmuir*, 2006, **22**, 7120-7123.
48 M. Bervas, L. C. Klein and G. G. Amatucci, *Journal of The Electrochemical Society*, 2006, **153**, A159.
49 Dan Ni, Wang Sun, Liqiang Xie, Qinghua Fan, Zhenhua Wang, Kening Sun, *Journal of Power Sources*, 2018, **374**, 166–174.
50 G.A. Giffin, *J. Mater. Chem. A*, 2016, **4**, 13378-13389
51 T. Torimoto, Y. Ohta, K. Enokida, D. Sugioka, T. Kameyama, T. Yamamoto, T. Shibayama, K. Yoshii, T. Tsuda, S. Kuwabata, *Journal of Materials Chemistry A*., 2015, **3**, 6177.
52 J.L. Anthony, J.L. Anderson, E.J. Maginn, J.F. Brennecke, *J. Phys. Chem. B*, 2005, **109**, 6366.
53 H. Himura, A. Irie, S. Masamune, *Transactions of the Materials Research Society of Japan*, 2011, **36**, 59.
54 A. Sergievskaya, A. Chauvin, S. Konstantinidis, *Beilstein J. Nanotechnol.*, 2022, **13**, 10.